Supplementary Information for

Emergent constraints on global soil moisture projections under climate change

Lei Yao[1,2], Guoyong Leng[1,*], Linfei Yu[1], Hongyi Li[3], Qiuhong Tang[1], Andre Python[3,4], Jim W. Hall[5], Xiaoyong Liao[1], Ji Li[1], Jiali Qiu[1], Johannes Quaas[6], Shengzhi Huang[7], Yin Jin[3], Jakob Zscheischler[8,9] and Jian Peng[10,11]

[1]Key Laboratory of Water Cycle and Related Land Surface Processes, Institute of Geographic Sciences and Natural Resources Research, Chinese Academy of Sciences, Beijing, China

[2]University of Chinese Academy of Sciences, Beijing, China

[3]Center for Data Science, Zhejiang University, Hangzhou, China

[4]Nuffield Department of Medicine, University of Oxford, Oxford, UK

[5]Environmental Change Institute, University of Oxford, Oxford, UK

[6]Leipzig Institute for Meteorology, Leipzig University, Leipzig, Germany

[7]State Key Laboratory of Eco-Hydraulics in Northwest Arid Region of China, Xi'an University of Technology, Xi'an, China

[8]Department of Computational Hydrosystems, Helmholtz Centre for Environmental Research—UFZ, Leipzig, Germany

[9]Technische Universität Dresden, Dresden, Germany

[10]Department of Remote Sensing, Helmholtz Centre for Environmental Research—UFZ, Leipzig, Germany

[11]Remote Sensing Centre for Earth System Research, Leipzig University, Leipzig, Germany

*Correspondence to Guoyong Leng (lenggy@igsnrr.ac.cn)

Contents of this file

Supplementary Note 1: Physical mechanisms underlying temperature and precipitation effect on soil moisture.

Following the Palmer Drought Severity Index (PDSI)[1] and the Budyko theory[2], soil moisture (SM) can be derived from water supply (precipitation, P) and water demand (potential evapotranspiration, PET). Physically, the climatic drivers of PET include net radiation (Rn), temperature (T), relative humidity (RH) and wind speed (WS) according to the FAO-Penman-monteith equation[3]. With the elevation of CO_2 concentrations, Rn tends to increase because of the extra longwave energy back to the surface, which leads to a direct increase in PET. At the same time, the warming (higher T) associated with more Rn could enhance PET by widening vapor pressure deficit, as saturation vapor pressure increases by 7%/°C according to the Clausius–Clapeyron law[4].

Projections based on CMIP6 models indicate a greater increase in Rn (9.2±2.6%) and T (6.2±1.7°C) over global land areas by the end of 21st century under the SSP5-8.5 scenario. However, changes in RH (-2.8±4.0%) and wind speed (-1.3±2.4%) are less pronounced, which suggests that future changes in PET are mainly driven by Rn and T (Supplementary Table 2). Here, we use T as a proxy of water demand instead of Rn, due to three reasons. First, we found a positive and statistically significant association between ΔT and ΔRn (r=0.71, p<0.05) and between ΔT and ΔET (r=0.60, p<0.05) (Supplementary Figure 7). Second, the observational uncertainty of T is substantially lower than Rn and model simulations (Supplementary Figure 20), which are the prerequisite for applying the EC approach[5]. This also explains why historical SM trend was not used to constrain ΔSM, despite a high correlation coefficient of 0.75 (Supplementary Figure 13). Third, only 9 models have provided outputs of Rn under the SSP5-8.5 scenario, which prohibit meaningful derivation of an emergent constraint of SM based on Rn.

Although ΔP does not appear to be associated with ΔSM, it shows a highly positive and significant correlation with ΔET (r=0.79, p<0.05), which is expected since the actual ET is also controlled by water supply from P. We also found significant correlations between ΔT and ΔP (r=0.82, p<0.05), which can be explained by atmospheric energetics[6]. Therefore, considering the effects of T and P interactions can greatly enhance the explaining capability of ΔSM. Indeed, when ΔT and ΔP are considered together, 67% of the variance of ΔSM can be explained, in contrast to 40% explained by ΔT alone. The remaining unexplained variance of ΔSM is associated with the effects of changes in vegetation structure and physiology[7], snow[8] CO_2[9] and etc.

The effect of T on SM is also supported by evidence from historical observations (Supplementary Table 4). Globally, a negative and significant correlation between the annual time series of T and SM is obtained based on the raw and detrended data of ERA5 (r=-0.86 and r=-0.51, respectively, p<0.05, Supplementary Table 10). Regionally, T plays a dominant role in semi-arid, dry sub-humid and humid zones, but not in hyper arid and arid regions where ET is mainly controlled by water supply (as indicated by P). In contrast, Rn and SM does not appear correlated when the datasets are detrended at the regional and global scales. Overall, the identified emergent relations in CMIP6 models are also detected in the observations with a determination of coefficients consistent with CMIP6 models (Supplementary Table 4).

Supplementary Note 2: Drivers of recent temperature and precipitation trends.

To quantify the drivers of recent T and P trends, we use CMIP6 model simulations with historical natural forcings (NAT) only, historical greenhouse gas (GHG) changes only, and all forcing agents combined (ALL)[10,11]. The effects of other anthropogenic (OANT) forcings are estimated by subtracting those under GHGs and NATs from those under ALL. Here, the simulations of five models (i.e., CanESM5, CESM2, E3SM-2-0, MRIOC6, and MRI-ESM2-0) that are available at the CMIP6 data archive (at https://esgf-node.llnl.gov/projects/cmip6/) are used for our analysis. Considering the potential impacts of climate internal variability (e.g., Interdecadal Pacific Oscillation, Pacific Decadal Oscillation, and Atlantic Multidecadal Oscillations), we also use their preindustrial control simulations with constant external forcings to estimate the influences of internal variability[12-14]. Here, we excluded the least-squares linear trend from each model's preindustrial control simulation to minimize the effect of model drift on the estimate of internal variability, following Yu et al. (2022)[15]. The results indicate that the observed T and P trends during 1980-2014 are mainly driven by external forcings of GHG emissions, with minor effects of aerosols and climate internal variability (Supplementary Figure 8).

Supplementary Method 1: Univariate linear constraint method

Building a univariate EC

By projecting the observed X and its uncertainty onto the X-axis through the emergent relationship, an observationally constrained Y with narrower uncertainty can be obtained, provided that the observational uncertainty of X is smaller than that of the simulated values[16,17]. The traditional EC (Eq. (S1)) has two major limitations: the assumption of a linear emergent relationship and the focus on a univariate constraint. Here, we used the historical T trend or P trend (1980-2014) as the predictor X, respectively, and ΔSM by the end of the century (2070-2099) as the predictand Y, where X and Y are N-dimensional vectors from N models.

$$Y = f\left(X\right) + \varepsilon = \beta_0 + \beta_1 X + \varepsilon \tag{S1}$$

where β_0 and β_1 are the intercept and slope, respectively, and ε is the N-dimensional random error with variance σ^2 which satisfies normality and homoscedasticity. The variance of the predicted response of the regression for a given x ($\sigma_y(x)$) can be obtained as follows Eq. (S2):

$$\sigma_y(x) = s\sqrt{1 + \frac{1}{N} + \frac{(x - \overline{X})^2}{N \cdot \sigma_X^2}} \tag{S2}$$

where s is the standard error of the residuals, which can be calculated by Eq. (S3); N is the number of models; σ_X^2 is the variance of X calculated by Eq. (S4); and $\overline{X}$ is the mean value of X.

$$s^2 = \frac{1}{N-2}\sum_{i=1}^{N}\left(f\left(x_i\right) - y_i\right)^2 \tag{S3}$$

$$\sigma_X = \sqrt{\frac{\sum_{i=1}^{N}(x_i - \overline{X})^2}{N}} \tag{S4}$$

Calculating the probability density of univariate EC

The probability density function (PDF) of ΔSM before constraint is derived from Eq. (S5), by assuming that all models are equally likely and sampled from a Gaussian distribution[18].

$$\mathrm{PDF}(y) = \frac{1}{\sqrt{2\pi \cdot \sigma_Y^2}} \exp\left\{ -\frac{(y-\overline{Y})^2}{2\sigma_Y^2} \right\} \tag{S5}$$

where σ_Y^2 is the variance of Y calculated by Eq. (S6); and $\overline{Y}$ is the mean value of Y.

$$\sigma_Y = \sqrt{\frac{\sum_{i=1}^{N}(y_i-\overline{Y})^2}{N}} \tag{S6}$$

The PDF of ΔSM after constraint is calculated following the Bayesian theorem, by numerically integrating $\mathrm{PDF}(y_{fu}|x_{ob})$ and $\mathrm{PDF}(x_{ob})$ (Eq. (S7)), where $\mathrm{PDF}(y_{fu}|x_{ob})$ means the probability density for the future projected variable y_{fu} given the historical observable variable x_{ob} (Eq. (S8)), and $\mathrm{PDF}(x_{ob})$ is the PDF for observational historical observable variable x_{ob}.

$$\mathrm{PDF}(y_{fu}) = \int_{-\infty}^{+\infty} \mathrm{PDF}(y_{fu} \mid x_{ob})\mathrm{PDF}(x_{ob})dx_{ob} \tag{S7}$$

$$\mathrm{PDF}(y \mid x) = \frac{1}{\sqrt{2\pi \cdot \sigma_y^2(x)}} \exp\left\{ -\frac{(y-f(x))^2}{2\sigma_y^2(x)} \right\} \tag{S8}$$

Supplementary Method 2: How to obtain the "prediction error" for a bivariate EC

In Eq. (7), *s* is the standard error of the residuals, which quantifies the overall "noise" or error in the data, and its square (s^2) is the variance in the residuals which reflects the goodness-of-fit of the regression model. The reason for using $N-p-1$ instead of $N-2$ in the denominator is to account for the degrees of freedom in the model, which represents the number of covariates of information used to estimate a parameter, and *p* is the number of covariates in the regression model. The term $N-p-1$ ensures that the variance estimate (s^2) is unbiased and provides a better estimation of the true variability in the data. The least-squares method used to fit the regression model remains valid for both LTP and NTP even in the presence of potential correlation between T and P. Since we only consider the outcome of the fitted model, the variance of the predicted response is therefore not affected by potential correlation between the covariates.

In Eq. (6), $\sigma_y(x_1,x_2) = s\sqrt{1+A\left(X^T X\right)^{-1} A^T}$ represents the variance of the predicted response of the regression model which is $Var\left(Y - A\hat{\beta} \mid A\right)$. The predicted response distribution is the predicted distribution of the residuals at the given point *A*, where *A* is an observational-based matrix $\begin{pmatrix}1 & x_1 & x_2\end{pmatrix}$ and $\begin{pmatrix}1 & x_1 & x_2 & x_1x_2\end{pmatrix}$ for LTP and NTP, respectively. Hence, we obtain the variance of the predicted response given *A* as follows:

$$\begin{aligned}
Var\left(Y - A\hat{\beta} \mid A\right) &= Var\left(Y \mid A\right) + Var\left(A\hat{\beta} \mid A\right) - 2Cov\left(Y, A\hat{\beta} \mid A\right) \\
&= Var\left(Y\right) + Var\left(A\hat{\beta} \mid A\right) \\
&= Var\left(Y\right) + A\,Var\left(\hat{\beta}\right) A^T \\
&= s^2 + s^2 A\left(X^T X\right)^{-1} A^T
\end{aligned} \tag{S9}$$

$Cov\left(Y, A\hat{\beta} \mid A\right)$ is zero by construction since the observational data is independent from the simulated data used to fit the regression model. We can also observe that $Var\left(Y\right)$ equals $Var\left(\varepsilon\right)$ which can be estimated by the least square error s^2 and the variance of the estimated $\hat{\beta}$ ($Var(\hat{\beta})$) can thus be expressed as $s^2\left(X^T X\right)^{-1}$. As long as the inverse matrix of $X^T X$ exists, the variance of the predicted response is not affected by the presence of correlation between the covariates.

Supplementary Table 1 The overall information of all available CMIP6 models in this study

Num	Models	Institution	Resolution	Historical	SSP1-2.6	SSP2-4.5	SSP3-7.0	SSP5-8.5	Reference
1	ACCESS-CM2	CSIRO	1.875°×1.25°	√	√	√	√	√	19
2	ACCESS-ESM1-5	CSIRO	1.875°×1.25°	√	√	√	√	√	20
3	BCC-CSM2-MR	BCC	1.125°×1.125°	√	√	√	√	√	21
4	CanESM5	CCCma	2.8125°×2.8125°	√	√	√	√	√	22
5	CanESM5-1	CCCma	2.8125°×2.8125°	√				√	22
6	CAS-ESM2-0	CAS	1.406°×1.406°	√	√	√	√	√	23
7	CESM2-WACCM	NCAR	1.25°×0.9375°	√	√	√	√	√	24
8	CMCC-CM2-SR5	CMCC	1.25°×0.9375°	√	√	√	√	√	25
9	CMCC-ESM2	CMCC	1.25°×0.9375°	√	√	√	√	√	26
10	E3SM-1-0	LLNL et al.,	1°×1°	√				√	27
11	E3SM-1-1	LLNL et al.,	1°×1°	√				√	27
12	E3SM-1-1-ECA	LLNL et al.,	1°×1°	√				√	27
13	EC-Earth3	EGU	0.70°×0.70°	√	√	√	√	√	28
14	EC-Earth3-CC	EGU	0.70°×0.70°	√		√		√	28
15	EC-Earth3-Veg	EGU	0.70°×0.70°	√	√	√	√	√	28
16	EC-Earth3-Veg-LR	EGU	1.125°×1.125°	√	√	√	√	√	28
17	FGOALS-f3-L	CAS	1.125°×1°	√	√	√	√	√	29
18	FGOALS-g3	CAS	2°×1.5°	√	√	√	√	√	30
19	FIO-ESM-2-0	FIO et al.,	1.25°×0.9375°	√	√	√		√	31
20	GFDL-ESM4	NOAA	1.25°×1°	√	√	√	√	√	32
21	IPSL-CM5A2-INCA	IPSL	3.75°×1.875°	√	√		√		33
22	IPSL-CM6A-LR	IPSL	2.5°×1.26°	√	√	√	√	√	34
23	KACE-1-0-G	NIMS	1.875°×1.25°	√	√	√	√	√	35
24	MIROC6	JAMSTEC	1.41°×1.41°	√	√	√	√	√	36
25	MPI-ESM1-2-HR	MPI	0.9375°×0.9375°	√	√	√	√	√	37
26	MPI-ESM1-2-LR	MPI	1.875°×1.875°	√	√	√	√	√	38
27	MRI-ESM2-0	MRI	1.125°×1.125°	√	√	√	√	√	39
28	NorESM2-LM	CICEO et al.,	2.5°×1.875°	√	√	√	√	√	40
29	NorESM2-MM	CICEO et al.,	1.25°×0.9375°	√	√	√	√	√	40
30	TaiESM1	RCEC	1.25°×0.9375°	√	√	√	√	√	41

Note: CSIRO: Commonwealth Scientific and Industrial Research Organization;

BCC: Beijing Climate Center;

CCCma: Canadian Centre for Climate Modelling and Analysis;

CAS: Chinese Academy of Sciences;

NCAR: National Center for Atmospheric Research;

CMCC: Fondazione Centro Euro-Mediterraneo sui Cambiamenti Climatici;

LLNL: Lawrence Livermore National Laboratory;

EGU: European Geosciences Union;

FIO: First Institute of Oceanography;

NOAA: National Oceanic and Atmospheric Administration;

IPSL: Institut Pierre Simon Laplace;

NIMS: National Institute of Meteorological Sciences;

JAMSTEC: Japan Agency for Marine-Earth Science and Technology;

MPI: Max Planck Institute for Meteorology;

MRI: Meteorological Research Institute;

CICEO: NorESM Climate Modeling Consortium consisting of CICERO;
RCEC: Research Center for Environmental Changes.

Supplementary Table 2 Future changes in driving factors of ΔET and ΔSM by 2070-2099 relative to 1980-2014. The means and standard deviations of CMIP6 models are shown.

		Mean	STD
Temperature	ΔT (°C)	6.21	1.70
Precipitation	ΔP (%)	11.75	4.60
Net radiation	ΔRn (%)	9.22	2.64
Relative humidity	ΔRH (%)	-2.80	3.96
Wind speed	ΔWS (%)	-1.32	2.40

Supplementary Table 3 Observed global temperature and precipitation datasets.

Name	Source	Spatial Resolution	Spatial Coverage	Temporal Resolution	Year	Climate Variable
HadCRU4	The CRU of the University of East Anglia	0.5°×0.5°	90N - 90S 0E - 360E	Monthly	1901-2021	T and P
Delaware V5.01	University of Delaware	0.5°×0.5°	89.75N - 89.75S 0.25E - 359.75E	Monthly	1900-2017	T and P
Berkeley	Berkeley Earth Surface Temperature Project	1°×1°	89.5N - 89.5S 0.5E - 359.5E	Monthly	1850-2022	T
GPCC	Global Precipitation Climatology Centre	0.25°× 0.25°	89.75N-89.75S 0.25E-359.75E	Monthly	1891-2019	P

Supplementary Table 4 Test of the emergent relations using historical soil moisture data. The determination of coefficients (R^2) is shown for the four types of emergent relations (LT, LP, LTP and NTP) using different observation datasets. The results based on detrended data are shown in brackets. * indicates statistical significance at 5% level.

Data		R^2			
T	P	LT	LP	LTP	NTP
CRU	CRU	0.7142*(0.2236*)	0.1695*(0)	0.7166*(0.2422*)	0.7303*(0.2683*)
Delaware	Delaware	0.6535*(0.2058*)	0.1156*(0.0524)	0.6626*(0.2293*)	0.6702*(0.2756*)
Berkeley	GPCC	0.7172*(0.2252*)	0.1529*(0.0002)	0.7198*(0.2448*)	0.7283*(0.2545*)

Supplementary Table 5 Observational and multi-model ensemble mean trends, uncertainty (defined as standard deviation, in brackets), and coefficient of variation (shown in the subsequent row) of the globe and five climate regions for 1980-2014.

Region	Temperature trend (°C/year)		Precipitation trend (mm/year)	
	Observation	MME	Observation	MME
Hyper arid	0.0346(±0.0037)	0.0414(±0.009)	0.227(±0.1797)	0.2076(±0.2167)
	10.76%	21.66%	79.13%	104.36%
Arid	0.0249(±0.001)	0.0363(±0.0077)	0.2812(±0.1443)	0.3494(±0.427)
	4.12%	21.32%	51.32%	122.21%
Semi-arid	0.0256(±0.0028)	0.0449(±0.0089)	0.5747(±0.1367)	0.7201(±0.3602)
	10.75%	19.8%	23.79%	50.02%
Dry sub-humid	0.0278(±0.0029)	0.0504(±0.0102)	0.5278(±0.131)	0.947(±0.4087)
	10.47%	20.31%	24.82%	43.15%
Humid	0.0283(±0.0023)	0.0456(±0.0113)	0.6078(±0.31)	0.8318(±0.4572)
	8.29%	24.7%	51.01%	54.97%
Global	0.0276(±0.0019)	0.0444(±0.0095)	0.5176(±0.1381)	0.7048(±0.2955)
	6.83%	21.34%	26.67%	41.93%

Supplementary Table 6 Uncertainty in observations and simulations of T, P, and their combinations.

	T	P	T+P	T+P+TxP
Obs	0.0520	0.2399	0.2814	0.4541
Simu	0.2172	0.4267	0.5729	1.1990
Obs/Simu	23.93%	56.23%	49.13%	37.87%

Supplementary Table 7 Regional ΔSM before and after constraints and the associated uncertainty.

ΔSM (±σ)	Before constraint (%)	After constraint (%)			
		LT	LP	LTP	NTP
Hyper arid	10.87(±23.39)	7.2(±24.05)	10.43(±24.25)	6.77(±24.5)	6.94(±24.09)
Hyper arid g	10.87(±23.39)	7.2(±24.05)	1.62(±19.99)	1.47(±20.47)	3.64(±19.98)
Arid	-0.68(±5.26)	-1.71(±5.6)	-0.67(±5.47)	-1.7(±5.71)	-1.83(±5.61)
Arid g	-0.68(±5.26)	-1.71(±5.6)	-2.24(±4.96)	-1.49(±5.19)	0.46(±4.74)
Semi-arid	-2.12(±4.48)	1.94(±4.55)	-2.35(±4.62)	2.13(±4.49)	3.27(±4.41)
Dry sub-humid	-3.37(±5.35)	2.61(±5.17)	-3.52(±5.64)	2.39(±5.09)	5.56(±5.13)
Humid	-6.03(±5.25)	-2.53(±5.09)	-5.97(±5.5)	-2.2(±5.17)	0.54(±4.88)

Supplementary Table 8 The NTP constraints on future ΔSM across different time periods and under different future scenarios.

Time	2020-2049				2035-2064			
Scenario	R^2	p	$\Delta\mu$	$\Delta\sigma$	R^2	p	$\Delta\mu$	$\Delta\sigma$
SSP1-2.6	0.38	<0.05	0.96%	-4.01%	0.30	<0.1	1.25%	2.08%
SSP2-4.5	0.37	<0.05	0.83%	-3.34%	0.30	<0.1	1.05%	1.51%
SSP3-7.0	0.40	<0.05	1.03%	-4.50%	0.33	<0.05	1.33%	0.37%
SSP5-8.5	0.37	<0.05	2.34%	-4.63%	0.36	<0.05	3.63%	-3.27%

Supplementary Table 9 Covariate coefficient (standardized) of the NTP method.

	X_1*X_2	X_1(T)	X_2(P)
Hyper arid	3.88	-9.94	-3.85
Arid	1.73	-5.39	-5.47
Semi-arid	1.07	-4.58	-4.06
Dry sub-humid	1.40	-6.64	-5.81
Humid	2.00	-8.01	-6.79
Global	1.53	-7.19	-5.88

Supplementary Table 10 Correlation coefficients between T, P, Rn, ET, and SM during the historical period 1980-2014. Numbers in the bracket are the results based on the detrended data. * indicates statistical significance at 5% level.

	Hyper arid	Arid	Semi-arid	Dry sub-humid	Humid	Global
T-SM	-0.49*(-0.22)	-0.75*(-0.25)	-0.72*(-0.32*)	-0.71*(-0.36*)	-0.84*(-0.59*)	-0.86*(-0.51*)
P-SM	0.59*(0.56*)	0.78*(0.84*)	0.71*(0.63*)	0.71*(0.52*)	0.23(0.14)	0.44*(0.21)
Rn-SM	0.11(0.19)	0.08(0.27)	-0.50*(-0.16)	-0.66*(-0.23)	-0.69*(-0.24)	-0.69*(-0.22)
T-ET	-0.11(0.02)	-0.41*(-0.13)	-0.01(0.21)	0.72*(0.49*)	0.85*(0.49*)	0.61*(0.44*)
P-ET	0.88*(0.88*)	0.96*(0.95*)	0.60*(0.60*)	-0.07(0.43*)	-0.15(0.02)	0.06(0.31*)
Rn-ET	0.51*(0.54*)	0.42*(0.50*)	0.14(0.28)	0.78*(0.60*)	0.92*(0.77*)	0.67*(0.53*)
Rn-T	0.18(0.14)	0.22(0.27)	0.76*(0.65*)	0.77*(0.53*)	0.86*(0.60*)	0.88*(0.74*)
T-P	-0.13(0.11)	-0.49*(-0.24)	-0.40*(-0.06)	-0.39*(0.02)	-0.05(0.17)	-0.28*(0.11)

Supplementary Table 11 Generalized climate classification scheme for Aridity Index values[42].

Aridity Index Value	Climate Class
<0.03	Hyper Arid
0.03-0.02	Arid
0.2-0.5	Semi-Arid
0.5-0.65	Dry sub-humid
>0.65	Humid

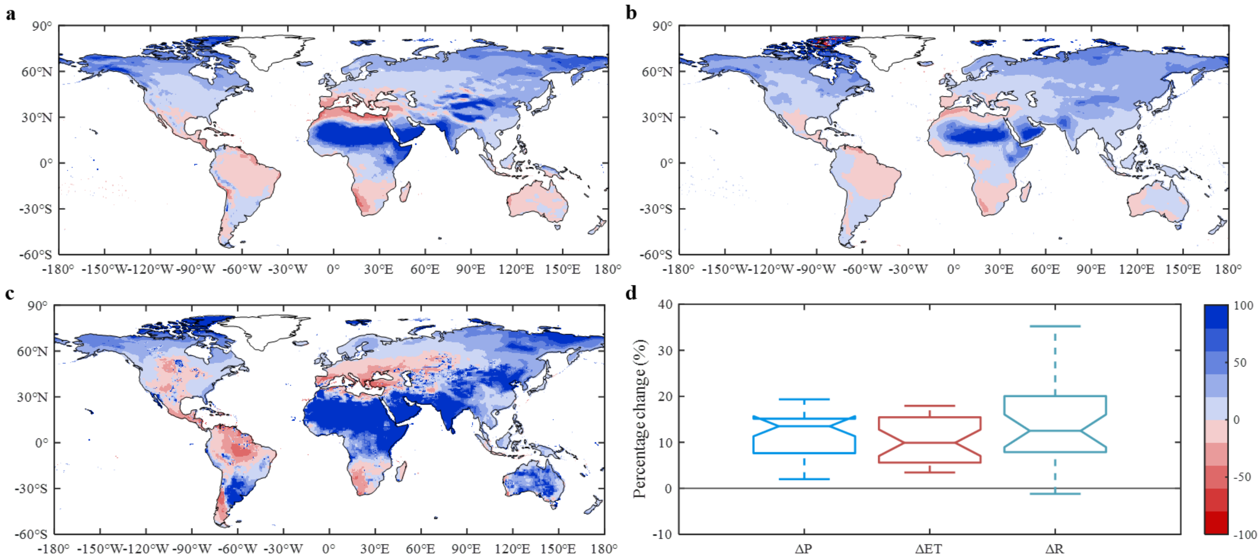

Supplementary Figure 1 Global ΔP, ΔET and ΔR by the end of the 21st century. a Spatial distribution of the multi-model ensemble mean of future ΔP (%) by 2070-2099 relative to 1980-2014. **b** and **c** the same as **b** but for changes in ΔET and ΔR, respectively. **d** Boxplots of global mean ΔP, ΔET, and ΔR based on CMIP6 outputs.

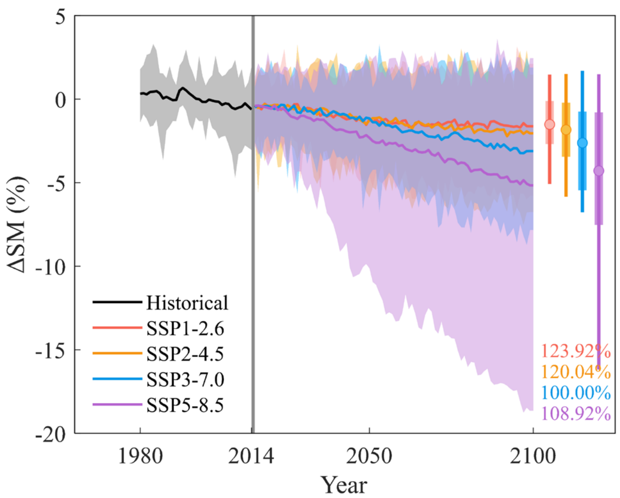

Supplementary Figure 2 Historical and future global ΔSM based on CMIP6 simulations. The shaded areas represent the range, and the solid lines are their mean values. The error bars on the right show the maximum, minimum and quartile values for 2070-2099. The coefficient of variation (CV) of each error bar is given on the bottom right in their individual colors.

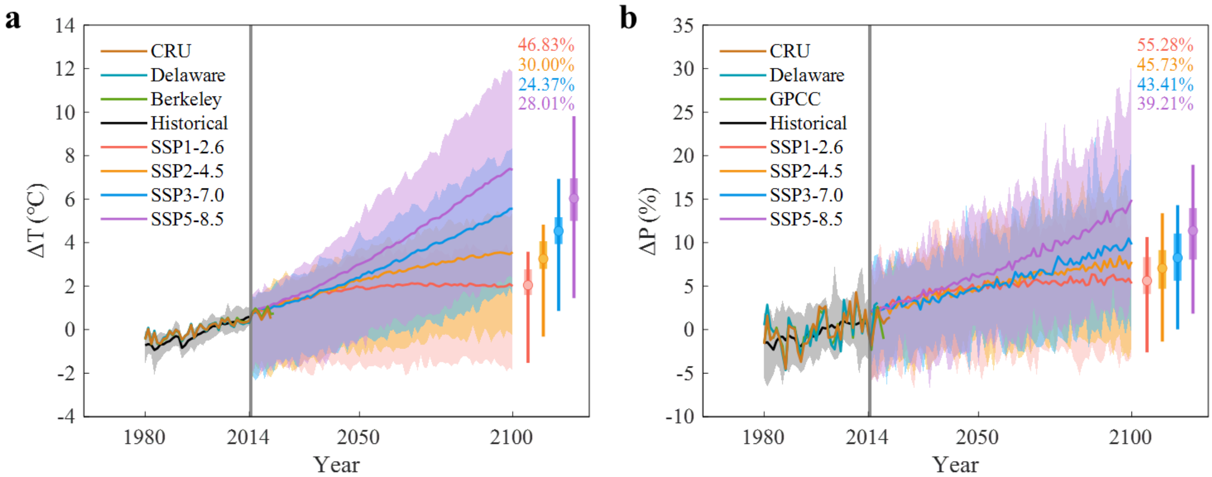

Supplementary Figure 3 Historical and future global annual ΔT and ΔP based on CMIP6 simulations. The same as Supplementary Figure 2, by for (**a**) ΔT and (**b**) ΔP, based on three observational datasets and outputs of 30 CMIP6 models, respectively.

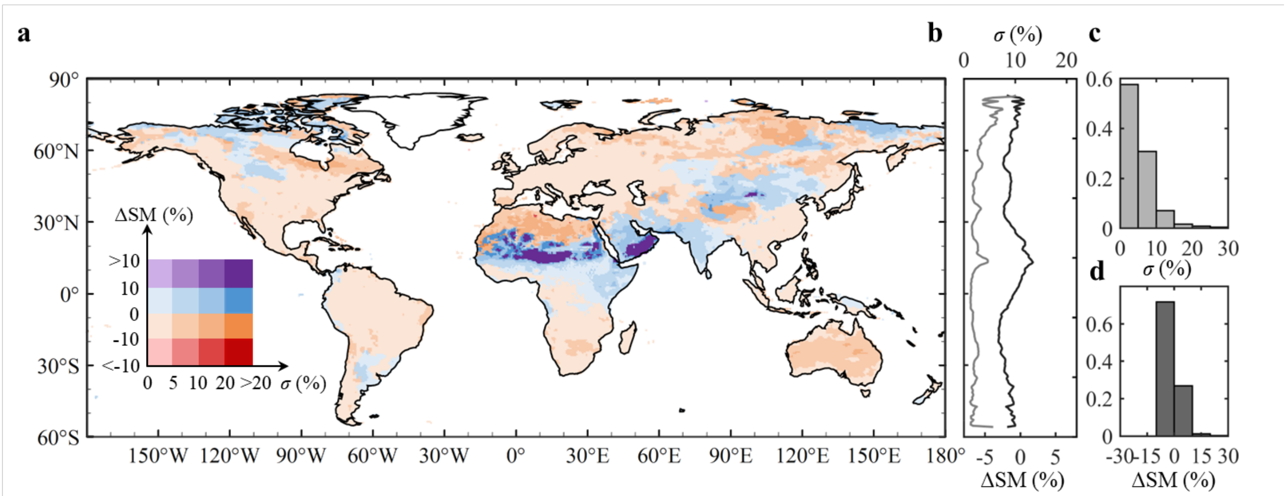

Supplementary Figure 4 Global ΔSM by the end of the 21st century under the SSP1-2.6 scenario and its uncertainty. a Spatial distribution of the multi-model ensemble mean of future ΔSM (%) by 2070-2099 relative to 1980-2014 and its uncertainty (inter-model standard deviation, σ) based on CMIP6 outputs (Supplementary Table. 1). **b** Latitudinal mean of ΔSM (black) and the associated uncertainty (gray). **c**, **d** Histogram (normalized scale of relative frequency) of grid-level σ and ΔSM across global land areas, respectively.

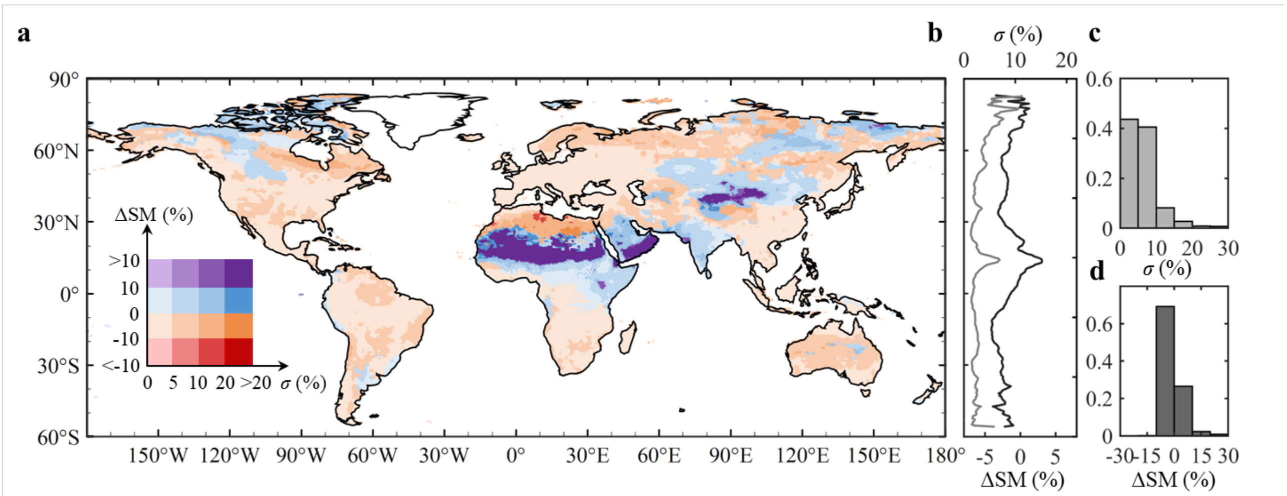

Supplementary Figure 5 Global ΔSM by the end of the 21st century under the SSP2-4.5 scenario and its uncertainty. The same as Supplementary Figure 4, but for the SSP2-4.5 scenario.

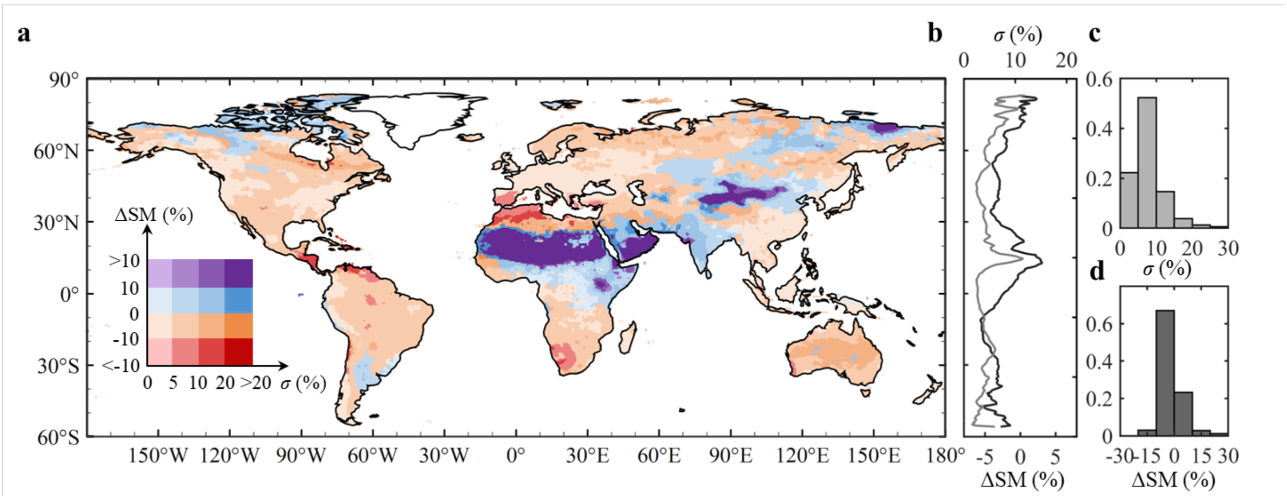

Supplementary Figure 6 Global ΔSM by the end of the 21st century under the SSP3-7.0 scenario and its uncertainty. The same as Supplementary Figure 4, but for the SSP3-7.0 scenario.

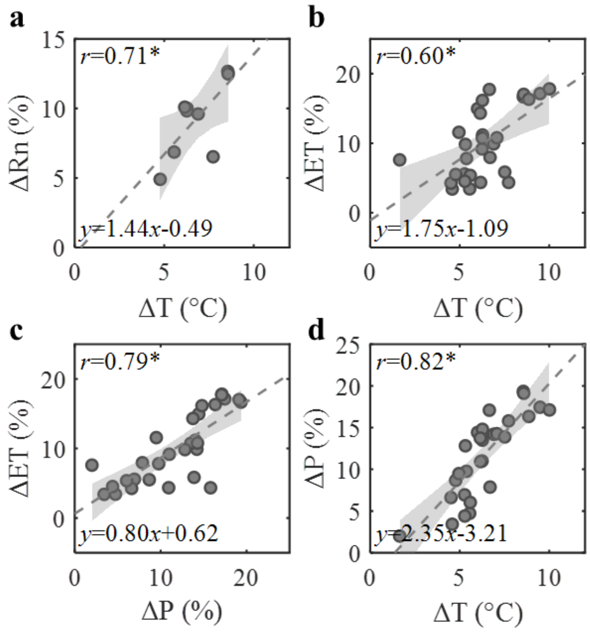

Supplementary Figure 7 Emergent relationships between future changes in temperature (ΔT), net radiation (ΔRn), precipitation (ΔP) and evapotranspiration (ΔET) under the SSP5-8.5 scenario based on CMIP6 output. a Relations between ΔT and ΔRn during 2070-2099 against 1980-2014. The dashed black line indicates the linear fitting line, with 95% confidence interval shown by shaded gray areas. The correlation coefficient (*r*) is shown on the top left, with * indicating statistically significant (p<0.05). **b**, **c**, and **d** The same as (**a**), but for relationships between ΔT and ΔET, ΔP and ΔET, ΔT and ΔP, respectively.

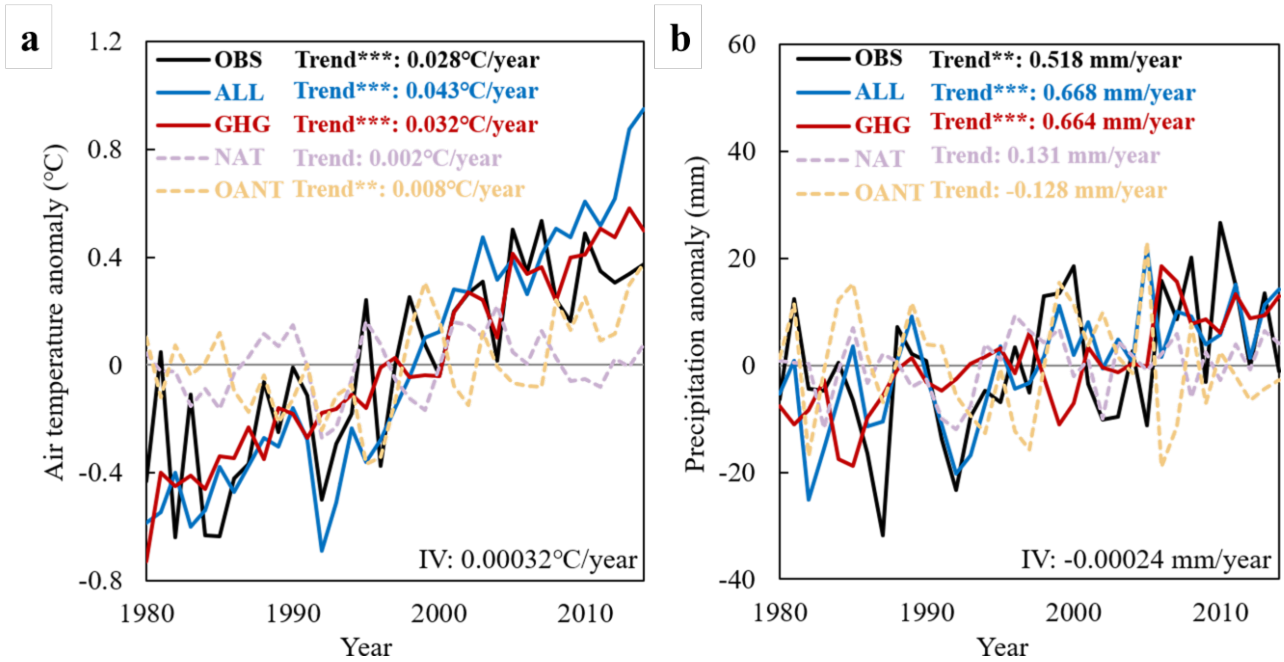

Supplementary Figure 8 Simulated and observational mean of global temperature and precipitation anomalies during 1980-2014. The multi-model ensemble mean result under ALL, GHG, NAT and OANT (other anthropogenic forcing agents) forcings are used for analysis. Note: *** indicates p<0.001; ** indicates p<0.01. IV indicates the effects of internal variability.

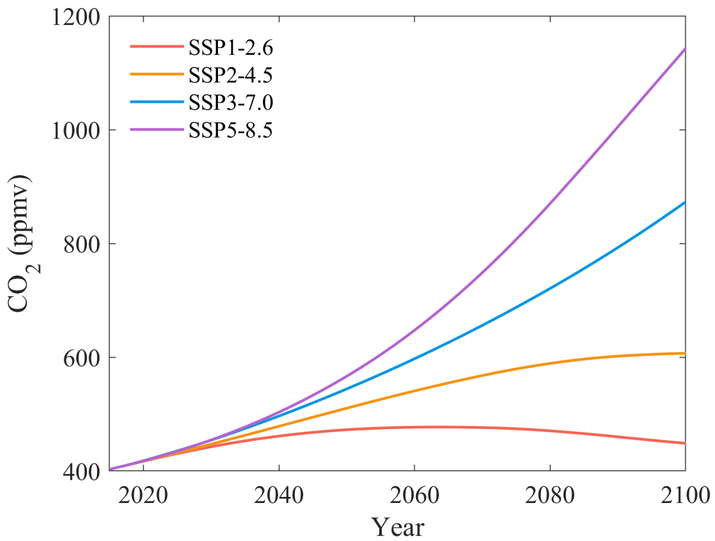

Supplementary Figure 9 Future annual emissions of CO_2 across four scenarios[43].

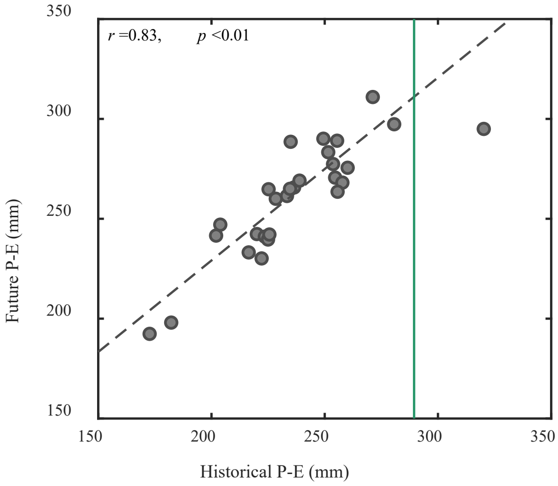

Supplementary Figure 10 Emergent relationship between historical and future surface available water (P-E). Each black dot corresponds to an ESM output. The dashed black line indicates the linear fitting line, with *r* and *p* shown on the top left. Observational P-E based on the ERA5 dataset is shown by the vertical green line.

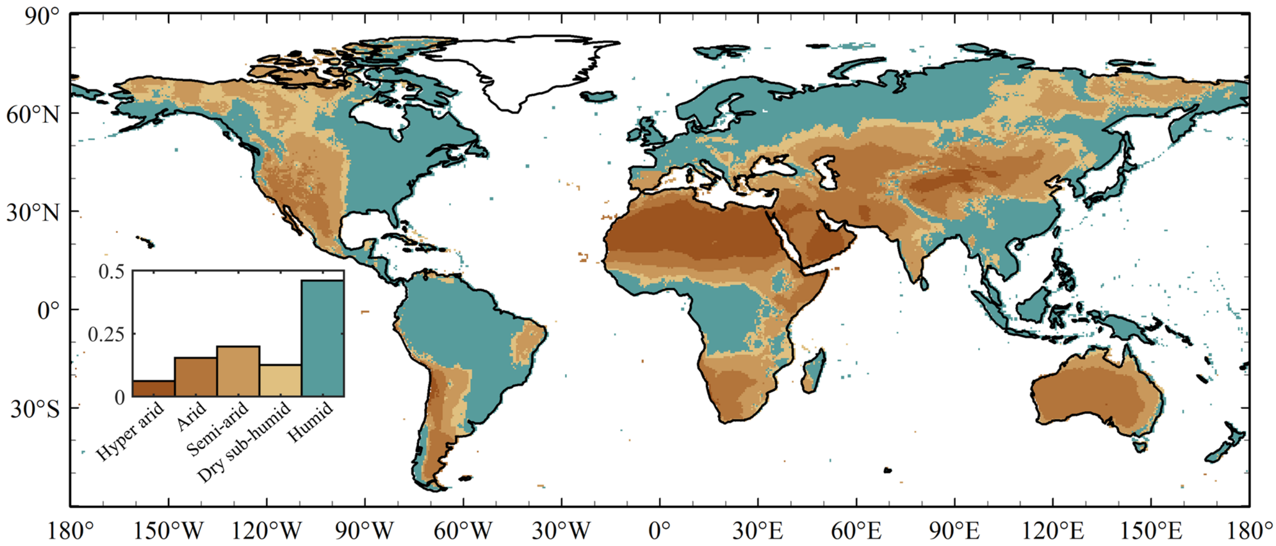

Supplementary Figure 11 Climate regions defined in this study and their corresponding frequency distribution (inset).

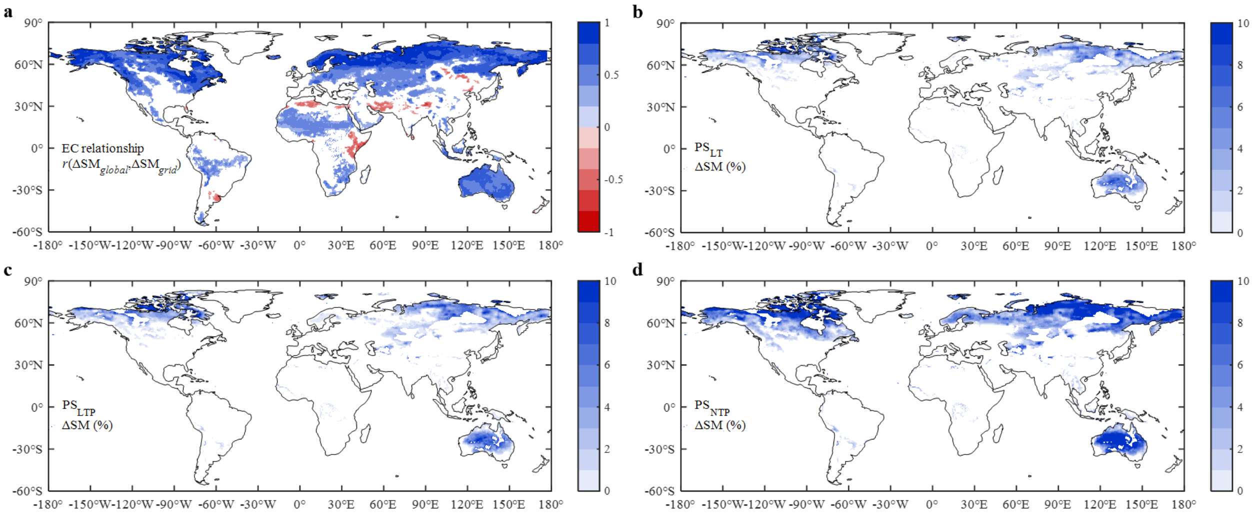

Supplementary Figure 12 Spatial distribution of ΔSM. a emergent relationships between global and grid-scale ΔSM, and only grids with significant relationships (p<0.05) are shown. **b** grid-scale ΔSM after LT constraint and only areas where the sign of ΔSM change from negative to positive are shown. **c** and **d** the same as (**b**) but for LTP and NTP constraints, respectively.

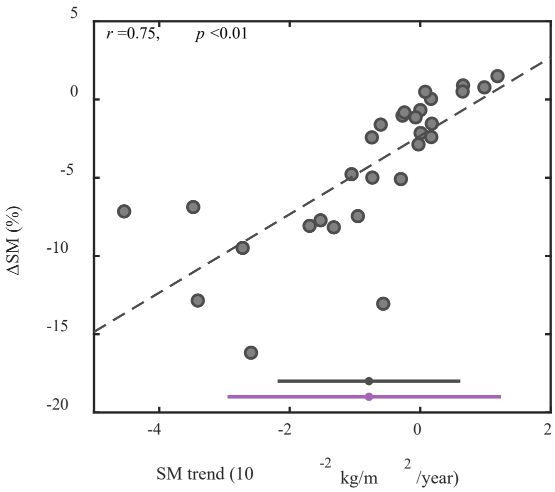

Supplementary Figure 13 Emergent relationship between historical SM trend and future ΔSM. Each black dot corresponds to an ESM output. The dashed black line indicates the linear fitting line, with r and p shown on the top left. The black and purple lines are uncertainties (mean±standard deviation) in SM trend simulations and observations, respectively.

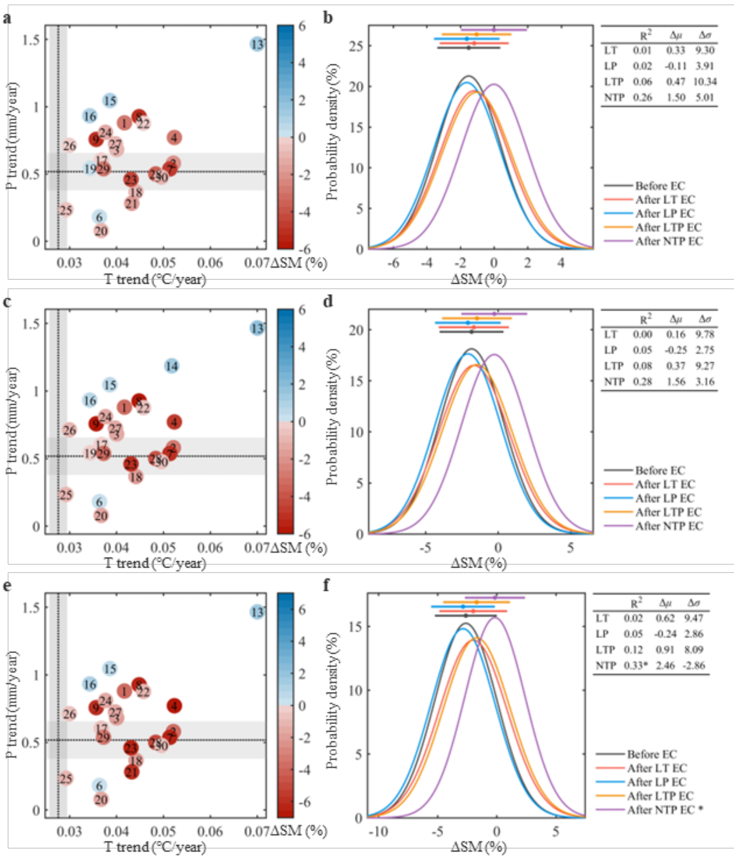

Supplementary Figure 14 Emergent constraints on global ΔSM across three future scenarios. a Each circle corresponds to a CMIP6 model (Supplementary Table 1), with simulated historical T trend plotted on the x-axis, P trend on the y-axis, and ΔSM under the SSP1-2.6 scenario indicated by color. The observational mean of T and P trends during the historical period are shown by the vertical and horizontal dotted lines, respectively, with the associated uncertainties indicated by the shading (±1 standard deviation) (Supplementary Table 3). **b** The probability density functions (PDFs) of future ΔSM before (black line) and after (colored lines) constraints. The red, blue, yellow, and purple lines are the PDFs of ΔSM after applying the EC of LT, LP, LTP and NTP, respectively. The corresponding error bars (mean ±1 standard deviation) are illustrated at the top. The star in the legend indicates that the PDF curves after constraint are significantly different (p<0.05) from that before constraints according to the Kolmogorov-Smirnov (K-S) test. The coefficients of determination (R^2) of the four ECs (* indicates p<0.05), the differences in the central estimate of ΔSM after constraint relative to that before constraint ($\Delta\mu=\mu_{after}-\mu_{before}$, %) and the differences in the associated uncertainties ($\Delta\sigma=(\sigma_{after}-\sigma_{before})/\sigma_{before}$, %) are given by the table inset. (**c, d**), (**e, f**) the same as (**a, b**), but for the SSP2-4.5 and SSP3-7.0 scenario, respectively.

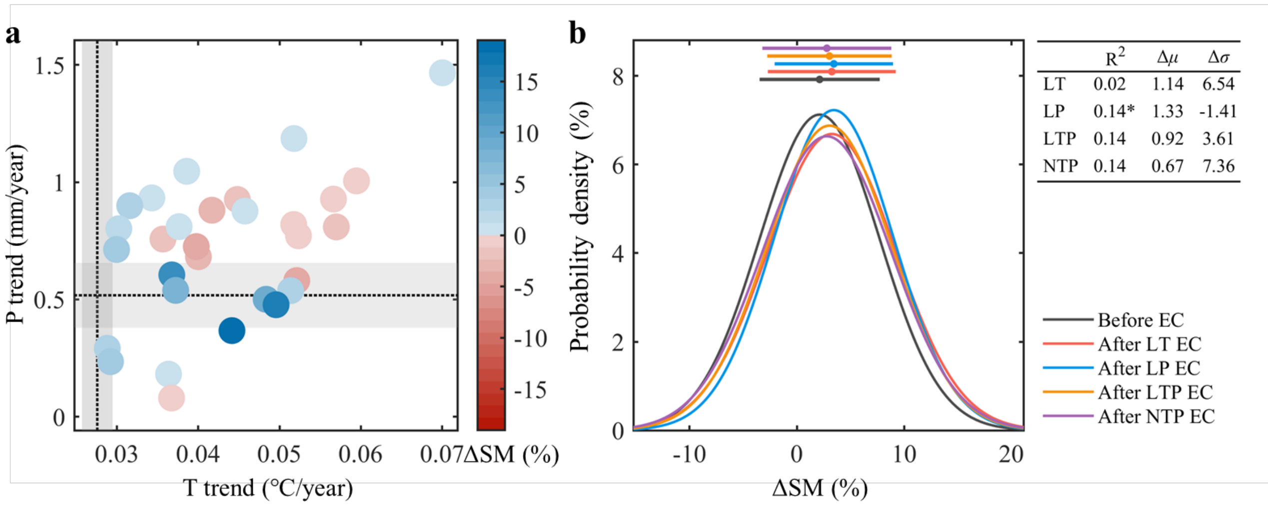

Supplementary Figure 15 Emergent constraints on global change in total soil moisture. The same as Supplementary Figure 14 but for changes in total soil moisture.

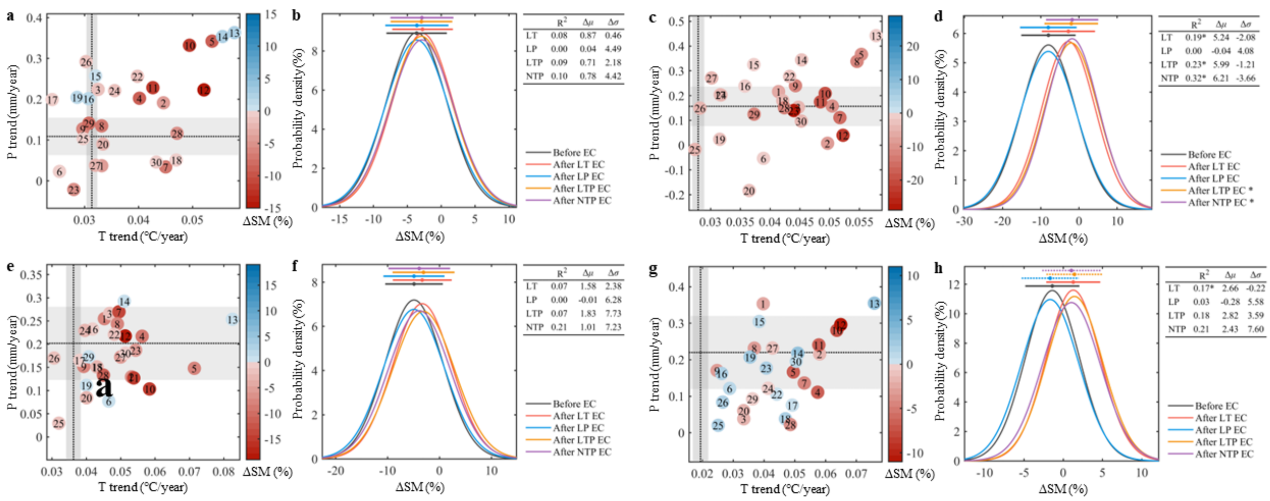

Supplementary Figure 16 Emergent constraints on global seasonal ΔSM. The same as Supplementary Figure 14 but for (**a, b**) spring, (**c, d**) summer, (**e, f**) autumn, and (**g, h**) winter seasons for the Northern Hemisphere.

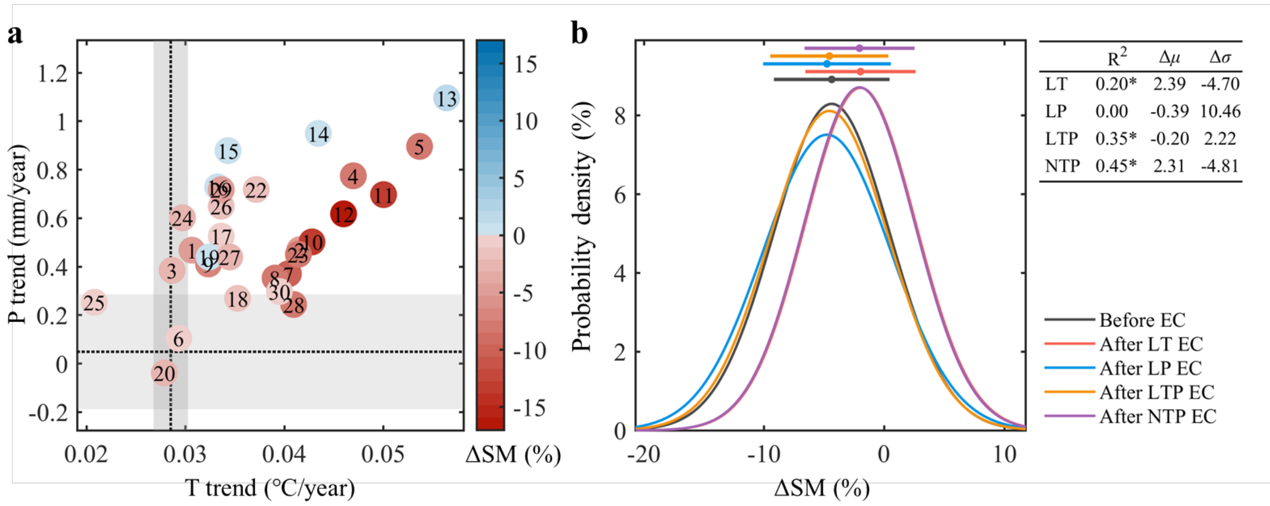

Supplementary Figure 17 Emergent constraints on global ΔSM. The same as Supplementary Figure 14 but using the historical period of 1970-2014.

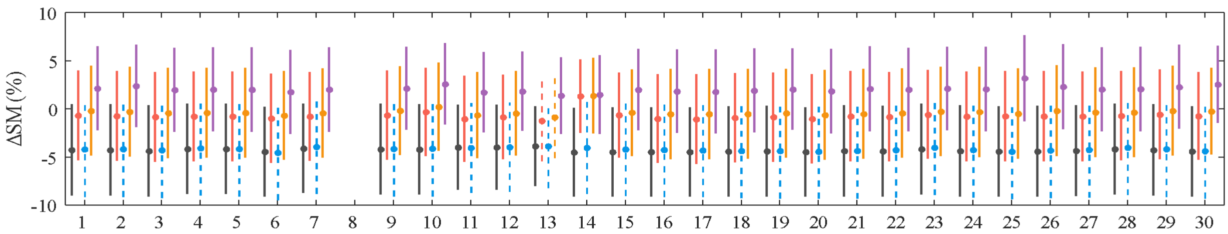

Supplementary Figure 18 The leave-one-out test for the emergent constraint of ΔSM. The black, red, blue, yellow, and purple lines are the error bars (with dots as mean and bars as ±1 standard deviation) associated with the estimation of ΔSM before and after applying the EC of LT, LP, LTP and NTP, respectively. A dotted line indicates that the relationship is not statistically significant (p>0.05), while solid lines denote significance with p<0.05.

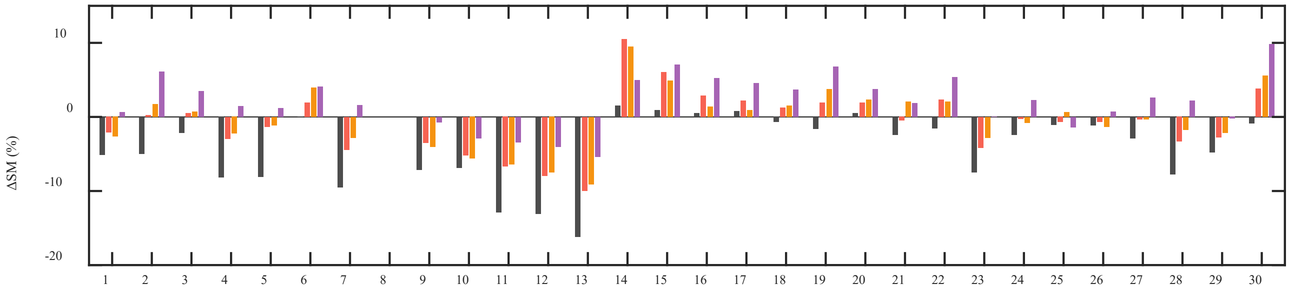

Supplementary Figure 19 ΔSM before and after constraints for each ESM. The black, red, yellow, and purple bars represent ΔSM before and after ECs with LT, LTP, and NTP, respectively. Results of LP EC were excluded due to their insignificance.

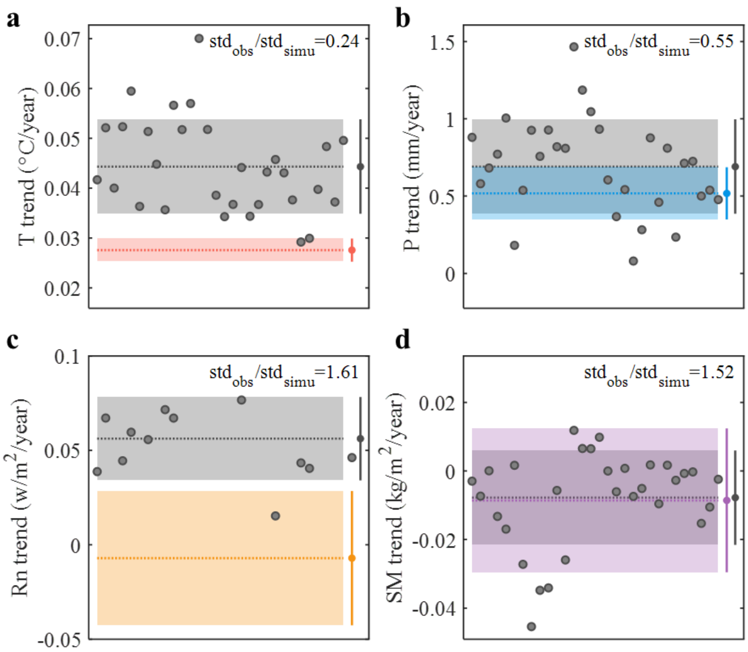

Supplementary Figure 20 Uncertainties in CMIP6 simulations and observations of historical trends of temperature (T), precipitation (P), radiation (Rn) and soil moisture (SM). a Scatters illustrate historical (1980-2014) T trend derived from 30 CMIP6 models. The mean of the models and observational datasets are represented by gray and colored dotted lines, respectively, with their uncertainties depicted by shaded gray and colored areas, respectively. Error bars of the two ensembles are shown on the right for comparison, the ratio of observational uncertainty to model uncertainty is displayed in the top-right corner. **b, c** and **d** The same as (**a**), but for uncertainties in historical trends of P, Rn, and SM, respectively.

Supplementary References

1 Palmer, W. C. *Meteorological Drought*. (Weather Bureau Research Paper No. 45, 1965).

2 Budyko, M. I., & Miller, D. H. *Climate and life*. Vol. 18 (Academic Pres, 1974).

3 Allen, R. G., Pereira, L. S., Raes, D., & Smith, M. *Crop evapotranspiration: guidelines for computing crop water requirements, fao irrigation and drainage paper 56*. (FAO, 56., 1998).

4 Held, I. M. & Soden, B. J. Robust responses of the hydrological cycle to global warming. *Journal of Climate* **19**, 5686-5699 (2006). https://doi.org/10.1175/JCLI3990.1

5 Hall, A., Cox, P., Huntingford, C. & Klein, S. Progressing emergent constraints on future climate change. *Nature Climate Change* **9**, 269-278 (2019). https://doi.org/10.1038/s41558-019-0436-6

6 Fläschner, D., Mauritsen, T. & Stevens, B. Understanding the Intermodel Spread in Global-Mean Hydrological Sensitivity*. *Journal of Climate* **29**, 801-817 (2016). https://doi.org/10.1175/jcli-d-15-0351.1

7 Vahmani, P., Jones, A. D. & Li, D. Will Anthropogenic Warming Increase Evapotranspiration? Examining Irrigation Water Demand Implications of Climate Change in California. *Earth's Future* **10** (2022). https://doi.org/10.1029/2021ef002221

8 Blankinship, J. C., Meadows, M. W., Lucas, R. G. & Hart, S. C. Snowmelt timing alters shallow but not deep soil moisture in the Sierra Nevada. *Water Resources Research* **50**, 1448-1456 (2014). https://doi.org/10.1002/2013wr014541

9 Yang, Y., Roderick, M. L., Zhang, S., McVicar, T. R. & Donohue, R. J. Hydrologic implications of vegetation response to elevated CO_2 in climate projections. *Nature Climate Change* **9**, 44-48 (2018). https://doi.org/10.1038/s41558-018-0361-0

10 Gillett, N. P. *et al.* The Detection and Attribution Model Intercomparison Project (DAMIP v1.0) contribution to CMIP6. *Geoscientific Model Development* **9**, 3685-3697 (2016). https://doi.org/10.5194/gmd-9-3685-2016

11 Eyring, V. *et al.* Overview of the Coupled Model Intercomparison Project Phase 6 (CMIP6) experimental design and organization. *Geoscientific Model Development* **9**, 1937-1958 (2016). https://doi.org/10.5194/gmd-9-1937-2016

12 Olonscheck, D. & Notz, D. Consistently Estimating Internal Climate Variability from Climate Model Simulations. *Journal of Climate* **30**, 9555-9573 (2017). https://doi.org/10.1175/jcli-d-16-0428.1

13 Resplandy, L., Séférian, R. & Bopp, L. Natural variability of CO_2 and O_2 fluxes: What can we learn from centuries-long climate models simulations? *Journal of Geophysical Research: Oceans* **120**, 384-404 (2015). https://doi.org/10.1002/2014jc010463

14 Roberts, C. D., Palmer, M. D., McNeall, D. & Collins, M. Quantifying the likelihood of a continued hiatus in global warming. *Nature Climate Change* **5**, 337-342 (2015). https://doi.org/10.1038/nclimate2531

15 Yu, L., Leng, G. & Tang, Q. Varying contributions of greenhouse gases, aerosols and natural forcings to Arctic land surface air temperature changes. *Environmental Research Letters* **17** (2022). https://doi.org/10.1088/1748-9326/aca2c3

16 Brient, F. Reducing Uncertainties in Climate Projections with Emergent Constraints: Concepts, Examples and Prospects. *Advances in Atmospheric Sciences* **37**, 1-15 (2019). https://doi.org/10.1007/s00376-019-9140-8

17 Chai, Y. *et al.* Using precipitation sensitivity to temperature to adjust projected global runoff. *Environmental Research Letters* **16** (2021). https://doi.org/10.1088/1748-9326/ac3795

18 Kwiatkowski, L. *et al.* Emergent constraints on projections of declining primary production in the tropical oceans. *Nature Climate Change* **7**, 355-358 (2017). https://doi.org/10.1038/nclimate3265

19 Bi, D. *et al.* Configuration and spin-up of ACCESS-CM2, the new generation Australian Community Climate and Earth System Simulator Coupled Model. *Journal of Southern Hemisphere Earth Systems Science* **70**, 225-251 (2020). https://doi.org/10.1071/es19040

20 Ziehn, T. *et al.* The Australian Earth System Model: ACCESS-ESM1.5. *Journal of Southern Hemisphere Earth Systems Science* **70**, 193-214 (2020). https://doi.org/10.1071/es19035

21 Wu, T. C., Min; Dong, Min; Fang, Yongjie; Jie, Weihua; Li, Jianglong; Li, Weiping; Liu, Qianxia; Shi, Xueli; Xin, Xiaoge; Yan, Jinghui; Zhang, Fang; Zhang, Jie; Zhang, Li; Zhang, Yanwu. BCC BCC-CSM2MR model output prepared for CMIP6 CMIP historical. (2018). https://doi.org/https://doi.org/10.22033/ESGF/CMIP6.2948

22 Swart, N. C. *et al.* The Canadian Earth System Model version 5 (CanESM5.0.3). *Geoscientific Model Development* **12**, 4823-4873 (2019). https://doi.org/10.5194/gmd-12-4823-2019

23 Zhang, H. *et al.* Description and Climate Simulation Performance of CAS‐ESM Version 2. *Journal of Advances in Modeling Earth Systems* **12** (2020). https://doi.org/10.1029/2020MS002210

24 Danabasoglu, G. NCAR CESM2-WACCM model output prepared for CMIP6 CMIP amip. (2019). https://doi.org/https://doi.org/10.22033/ESGF/CMIP6.10041

25 Nicolì, D. B., Alessio. CMCC CMCC-CM2-SR5 model output prepared for CMIP6 DCPP. (2023). https://doi.org/https://www.wdc-climate.de/ui/entry?acronym=C6_4368434

26 Lovato, T. *et al.* CMIP6 Simulations With the CMCC Earth System Model (CMCC‐ESM2). *Journal of Advances in Modeling Earth Systems* **14** (2022). https://doi.org/10.1029/2021ms002814

27 Bogenschutz, P. A. *et al.* The E3SM version 1 single-column model. *Geoscientific Model Development* **13**, 4443-4458 (2020). https://doi.org/10.5194/gmd-13-4443-2020

28 Döscher, R. *et al.* The EC-Earth3 Earth system model for the Coupled Model Intercomparison Project 6. *Geoscientific Model Development* **15**, 2973-3020 (2022). https://doi.org/10.5194/gmd-15-2973-2022

29 He, B. *et al.* CAS FGOALS-f3-L Model Datasets for CMIP6 Historical Atmospheric Model Intercomparison Project Simulation. *Advances in Atmospheric Sciences* **36**, 771-778 (2019). https://doi.org/10.1007/s00376-019-9027-8

30 Li, L. *et al.* The Flexible Global Ocean‐Atmosphere‐Land System Model Grid‐Point Version 3 (FGOALS‐g3): Description and Evaluation. *Journal of Advances in Modeling Earth Systems* **12** (2020). https://doi.org/10.1029/2019ms002012

31 Bao, Y., Song, Z. & Qiao, F. FIO‐ESM Version 2.0: Model Description and Evaluation. *Journal of Geophysical Research: Oceans* **125** (2020). https://doi.org/10.1029/2019jc016036

32 Dunne, J. P. *et al.* The GFDL Earth System Model Version 4.1 (GFDL‐ESM 4.1): Overall Coupled Model Description and Simulation Characteristics. *Journal of Advances in Modeling Earth Systems* **12** (2020). https://doi.org/10.1029/2019ms002015

33 Sepulchre, P. *et al.* IPSL-CM5A2 – an Earth system model designed for multi-millennial climate simulations. *Geoscientific Model Development* **13**, 3011-3053 (2020). https://doi.org/10.5194/gmd-13-3011-2020

34 Boucher, O. *et al.* Presentation and Evaluation of the IPSL‐CM6A‐LR Climate Model. *Journal of Advances in Modeling Earth Systems* **12** (2020). https://doi.org/10.1029/2019ms002010

35 Byun, Y.-H. L., Yoon-Jin; Sung, Hyun Min; Kim, Jisun; Sun, Minah; Kim, Byeong-Hyeon. NIMS-KMA KACE1.0-G model output prepared for CMIP6 CMIP amip. (2019). https://doi.org/https://doi.org/10.22033/ESGF/CMIP6.8350

36 Tatebe, H. *et al.* Description and basic evaluation of simulated mean state, internal variability, and climate

sensitivity in MIROC6. *Geoscientific Model Development* **12**, 2727-2765 (2019). https://doi.org/10.5194/gmd-12-2727-2019

37 Müller, W. A. *et al.* A Higher‐resolution Version of the Max Planck Institute Earth System Model (MPI‐ESM1.2‐HR). *Journal of Advances in Modeling Earth Systems* **10**, 1383-1413 (2018). https://doi.org/10.1029/2017ms001217

38 Mauritsen, T. *et al.* Developments in the MPI‐M Earth System Model version 1.2 (MPI‐ESM1.2) and Its Response to Increasing CO2. *Journal of Advances in Modeling Earth Systems* **11**, 998-1038 (2019). https://doi.org/10.1029/2018ms001400

39 Yukimoto, S. *et al.* The Meteorological Research Institute Earth System Model Version 2.0, MRI-ESM2.0: Description and Basic Evaluation of the Physical Component. *Journal of the Meteorological Society of Japan. Ser. II* **97**, 931-965 (2019). https://doi.org/10.2151/jmsj.2019-051

40 Seland, Ø. *et al.* Overview of the Norwegian Earth System Model (NorESM2) and key climate response of CMIP6 DECK, historical, and scenario simulations. *Geoscientific Model Development* **13**, 6165-6200 (2020). https://doi.org/10.5194/gmd-13-6165-2020

41 Lee, W.-L. *et al.* Taiwan Earth System Model Version 1: description and evaluation of mean state. *Geoscientific Model Development* **13**, 3887-3904 (2020). https://doi.org/10.5194/gmd-13-3887-2020

42 Zomer, R. J., Xu, J. & Trabucco, A. Version 3 of the Global Aridity Index and Potential Evapotranspiration Database. *Scientific Data* **9** (2022). https://doi.org/10.1038/s41597-022-01493-1

43 Cheng, W. *et al.* Global monthly gridded atmospheric carbon dioxide concentrations under the historical and future scenarios. *Scientific Data* **9** (2022). https://doi.org/10.1038/s41597-022-01196-7